Multi-site transfer function approach for real-time modeling of the ground electric field induced by laterally-nonuniform ionospheric source

Mikhail Kruglyakov[1,2], Elena Marshalko[3], Alexey Kuvshinov[2], Maxim Smirnov[4], and Ari Viljanen[3]

[1]University of Otago, Dunedin, New Zealand
[2]Institute of Geophysics, ETH Zürich, Zürich, Switzerland
[3]Finnish Meteorological Institute, Helsinki, Finland
[4]Lulea University of Technology, Lulea, Sweden

Key Points:

- Multi-site transfer function approach is proposed for real-time modeling of the ground electric field induced by laterally-nonuniform source
- The approach exploits magnetic field data from multiple locations and spatial modes describing the ionospheric source
- Good agreement between modeled and observed GEF and GIC is demonstrated

Corresponding author: Mikhail Kruglyakov, mikhail.kruglyakov@otago.ac.nz

Abstract

We propose a novel approach to model the ground electric field (GEF) induced by laterally-nonuniform ionospheric sources in the real-time. The approach exploits the multi-site transfer function concept, continuous magnetic field measurements at multiple sites in the region of interest, and spatial modes describing the ionospheric source. We compared the modeled GEFs with those measured at two locations in Fennoscandia and observed good agreement between modeled and measured GEF. Besides, we compared GEF-based geomagnetically induced current (GIC) with that measured at the Mäntsälä natural gas pipeline recording point and again observed remarkable agreement between modeled and measured GIC.

Plain Language Summary

The Earth's magnetic field disturbances, like geomagnetic storms and magnetospheric substorms, generate geomagnetically induced currents (GIC) in technological systems like power grids. GIC calculation is of practical interest since, in some cases, GIC can cause power grid blackouts. An accurate GIC calculation, preferably in real-time, requires knowledge of the ground electric field (GEF) along power lines. The GEF is rarely measured directly, so it needs to be simulated using, as realistic as possible, models of the Earth's electrical conductivity and the source responsible for geomagnetic disturbances. This study presents and validates a novel approach to model the GEF in real-time, which exploits – in a non-conventional way – magnetic field measurements at multiple sites in the region of interest.

1 Introduction

According to Faraday's law, the large fluctuations of the Earth's magnetic field during geomagnetic storms and magnetospheric substorms generate the ground electric field (GEF), which in turn drives the so-called geomagnetically induced currents (GIC) in ground-based technological systems, such as power grids and pipelines (Viljanen & Pirjola, 1994). GIC calculation is of practical interest since, in the worst case, GIC can cause the transformers' destructions lead to power grid blackouts, as it happened, for example, in the Malmö region in Sweden on 30 October 2003 (Pulkkinen et al., 2005) and in Otago region in New Zealand on 6 November 2001(Marshall et al., 2012; Rodger et al., 2017). An accurate calculation of GIC variations, ideally in real-time, requires knowledge of the spatio-temporal evolution of ground electric field (GEF) along power/pipelines. However, GEF measurements are occasional and, if they exist, usually last a few months at most. So the only alternative is the numerical simulation of the GEF.

The majority of the studies in connection with GEF or GIC simulations are based on the simplest model of the source, i.e. the laterally uniform one, and, often, but not always, on the laterally uniform conductivity distribution model (e.g. Wang et al. (2016); Divett et al. (2017); Kelbert et al. (2017); Bailey et al. (2018); Nakamura et al. (2018); Marshall et al. (2019); Rosenqvist and Hall (2019); Divett et al. (2020)).The intermediate approach for the use of a non-uniform source without the full simulations for one is used in (Viljanen et al., 2012), (Campanyà et al., 2019) and (Malone-Leigh et al., 2023), where the relations between electric and magnetic fields are based on plane-wave assumption, while the magnetic field is obtained by the interpolation from few observation sites. As for the full simulations with non-uniform sources, there are just a few of them (e.g. Beggan (2015); Honkonen et al. (2018); Marshalko et al. (2020, 2021); Beggan et al. (2021)).

Very recently Kruglyakov, Kuvshinov, and Marshalko (2022) proposed a method for real-time modeling of the GEF induced by laterally-varying ionospheric sources. Their technique is based on the isolation of the inducing source (approximated by ionospheric sheet current) using the Spherical Elementary Current System (SECS) approach (Vanhamäki

& Juusola, 2020) as applied to the magnetic field variations simultaneously recorded at a regional network of observations. Further, the source is factorized by spatial modes (SM) and respective time-varying expansion coefficients using time-domain Principal Component Analysis (PCA) of SECS-recovered inducing current.

The SECS approach can be viewed as a regional variant of the Gauss method — the method used to separate the inducing and induced signals on a global scale. If the region of interest is characterized by 3-D conductivity distribution, the induced part is inevitably influenced by 3-D effects arising, particularly from the lateral (for example, land/ocean) conductivity contrasts. Given the usually deficient spatial distribution of the magnetic field observations, the SECS approach precludes an accurate description of the induced part affected by localized 3-D effects. Such imperfection in the induced part description also influences the recovery of the inducing part in terms of the recovery of the time series of expansion coefficients.

To circumvent this problem Marshalko et al. (2023) introduced an approach to estimate expansion coefficients more accurately. The approach also exploits the spatial modes resulting from the PCA of SECS-recovered inducing source, but an estimation of the expansion coefficients is performed using a 3-D conductivity model of the region. However, the disadvantage of their method is a high computational load to obtain expansion coefficients, thus precluding its implementation for real-time GEF modeling.

This paper proposes a method that also works with spatial modes but avoids estimating the expansion coefficients. An approach is based on the multi-site (MS) transfer function (TF) concept where MS TF relate the GEF at any location with a horizontal components of magnetic field at (fixed) multiple locations. Notably, an approach allows researchers to model the GEF in real time. The proposed technique can be considered a generalization of the inter-site TF formalism presented in (Kruglyakov, Kuvshinov, & Nair, 2022). In their paper, TFs relate sea-bed and single-site land-based magnetic fields, and spatial modes are obtained from spherical harmonic analysis of the magnetic data recorded at a global network of geomagnetic observatories.

Using Fennoscandia as a study region, we validate the MS TF approach by comparing modeled and measured GEF and GIC time series. The reasons for selecting this high-latitude region are manifold. First, technological systems in polar regions are especially vulnerable due to the excessive GIC. Second, the inducing source at high latitudes reveals significant lateral variability, which we are interested in accounting for in our approach. Third, the 3-D electrical conductivity model is available for Fennoscandia (Korja et al., 2002). Fourth, there is a magnetometer network in the region (International Monitor for Auroral Geomagnetic Effect, IMAGE (Tanskanen, 2009)), which provides long-term, simultaneous and continuous measurements of the magnetic field at multiple locations — the prerequisite data for successfully applying the proposed approach. Moreover, in Fennoscandia, one can find relatively long (from weeks to months) continuous GEF measurements performed during magnetotelluric surveys in the region. Finally, GIC observations have been carried out at the Mäntsälä natural gas pipeline recording point starting from November 1998 (Viljanen et al., 2006), allowing us to compare observed and modeled GIC for several space weather events.

2 Methodology

We assume that the horizontal ground electric field $\mathbf{E}_h = (E_x, E_y)$ at any location is related in the frequency domain to $\mathbf{B}_h = (B_x, B_y)$ at N sites as

$$\mathbf{E}_h(\mathbf{r}, \omega; \sigma) = \sum_{k=1}^{N} \Lambda(\mathbf{r}, \mathbf{r}_k, \omega; \sigma) \mathbf{B}_h(\mathbf{r}_k, \omega; \sigma), \tag{1}$$

where x and y are directed to geographic North and East, respectively.

A set of $\Lambda_k \equiv \Lambda(\mathbf{r}, \mathbf{r}_k, \omega; \sigma)$ is called multi-site transfer function, where each Λ_k is the following 2×2 matrix

$$\Lambda_k = \begin{pmatrix} \Lambda_{xx,k} & \Lambda_{xy,k} \\ \Lambda_{yx,k} & \Lambda_{yy,k} \end{pmatrix}. \tag{2}$$

Estimating the elements of matrices Λ_k, $k = 1, 2, \ldots, N$ at a given frequency ω and conductivity model σ is performed as follows. First, one calculates the fields $\mathbf{B}^{(l)}(\mathbf{r}_k, \omega; \sigma)$ and $\mathbf{E}^{(l)}(\mathbf{r}, \omega; \sigma)$ corresponding to l-th spatial modes $\mathbf{j}_l(\mathbf{r})$ describing the inducing (extraneous) source

$$\mathbf{j}^{\text{ext}}(\mathbf{r}, t) = \sum_{l=1}^{L} c_l(t)\mathbf{j}_l(\mathbf{r}), \tag{3}$$

where L stands for a number of spatial modes. Then the elements of Λ_k are estimated row-wise using the calculated $\mathbf{B}_h^{(l)}$ and $\mathbf{E}_h^{(l)}$ fields. Specifically, elements of Λ_k are obtained as the solution of the following two systems of linear equations (SLE)

$$\Lambda_{xx,1}B_x^{(l)}(\mathbf{r}_1) + \Lambda_{xy,1}B_y^{(l)}(\mathbf{r}_1) + \cdots + \Lambda_{xx,N}B_x^{(l)}(\mathbf{r}_N) + \Lambda_{xy,N}B_y^{(l)}(\mathbf{r}_N) = E_x^{(l)}(\mathbf{r}), \tag{4}$$

and

$$\Lambda_{yx,1}B_x^{(l)}(\mathbf{r}_1) + \Lambda_{yy,1}B_y^{(l)}(\mathbf{r}_1) + \cdots + \Lambda_{yx,N}B_x^{(l)}(\mathbf{r}_N) + \Lambda_{yy,N}B_y^{(l)}(\mathbf{r}_N) = E_y^{(l)}(\mathbf{r}), \tag{5}$$

where $l = 1, 2, \ldots, L$. Note, that in Equations (4) and (5) the dependency of all quantities on ω, $\mathbf{B}_h^{(l)}$ and $\mathbf{E}_h^{(l)}$ on σ, and elements of Λ_k on σ, $\mathbf{r}$ and $\mathbf{r}_k$ are omitted but implied. To resolve the TF, the number of spatial modes, L, should be equal to or larger than the doubled number of the sites, N, i.e. $L \geq 2N$. Also, our model experiments indicate that the condition number of the system matrices in Equations (4) and (5) can be quite large, so we used the regularized ordinary least squares approach to solve the above SLEs.

Once elements of Λ_k are estimated at a predefined number of frequencies, the GEF at a given time instant $t_i = i\Delta t$ and a given location $\mathbf{r}$ is then calculated using a numerical scheme similar to that described by Marshalko et al. (2023)(cf. Equation 20 of that paper), namely

$$\mathbf{E}_h(\mathbf{r}, t_i; \sigma) = \sum_{n=0}^{N_t}\sum_{k=1}^{N} \Lambda^{(n)}(\mathbf{r}, \mathbf{r}_k, T_\Lambda; \sigma)\mathbf{B}_h^{\text{obs}}(\mathbf{r}_k, t_i - n\Delta t), \tag{6}$$

where $\mathbf{B}_h^{\text{obs}}$ stands for horizontal components of the observed field in corresponding locations and $N_t = T_\Lambda/\Delta t$. As discussed in (Marshalko et al., 2023), computation of quantities like $\Lambda^n(\mathbf{r}, \mathbf{r}_k, T_\Lambda; \sigma)$ can be reduced to the estimation of the following integrals

$$\Lambda^{(n)}(\mathbf{r}, \mathbf{r}_k, T_\Lambda; \sigma) = \text{Re}\left\{ \frac{\Delta t}{\pi} \int_0^{\frac{\pi}{\Delta t}} \Lambda(\mathbf{r}, \mathbf{r}_k, \omega; \sigma) e^{-i\omega n \Delta t} d\omega \right\}, \; n = 1, 2, \ldots, N_\Lambda - 1. \tag{7}$$

Expressions for $\Lambda^{(0)}$ and Λ^{N_Λ} are more complicated, but their calculation is similar to that presented in Appendix A of (Marshalko et al., 2023) to calculate the corresponding terms for the electric field.

Computation of the integrals in Equation (7) is performed as follows. First, $\Lambda(\mathbf{r}, \mathbf{r}_k, \omega; \sigma)$ are computed at N_f logarithmically spaced frequencies from $f_{\min}$ to $f_{\max}$ using Equations (4) and (5). Further, one can analytically compute the corresponding integrals by exploiting cubic spline interpolation as applied to calculated Λ. Our model experiments (not shown in the paper) indicate that $N_f = 71$, $f_{\min} = 6.13{\cdot}10^{-7}$ Hz, and $f_{\max} = 0.054$ Hz provide an accurate estimation of the integrals, in the assumption that Δt is taken as 10 s.

As seen from Equations (4) and (5), the estimation of $\Lambda(\mathbf{r}, \mathbf{r}_k, \omega; \sigma)$ requires specification of $\mathbf{j}_l, l = 1, 2, \ldots, L$. The form of $\mathbf{j}_l$ (and their number, L) varies with the application. As discussed in Introduction, in this paper, we use spatial modes obtained by means of the time-domain Principal Component Analysis (PCA) of the SECS-recovered inducing source. The reader can find further details on the derivation of these modes in the next section.

As also seen from Equations (4) and (5) (and already mentioned before), the estimation of $\Lambda(\mathbf{r}, \mathbf{r}_k, \omega; \sigma)$ implies computations of $\mathbf{B}^{(l)}(\mathbf{r}_k, \omega; \sigma)$ and $\mathbf{E}^{(l)}(\mathbf{r}, \omega; \sigma)$ in a given conductivity model σ of the region of interest. We performed these computations using the scalable 3-D EM forward modeling code PGIEM2G (Kruglyakov & Kuvshinov, 2018) based on a method of volume integral equation.

Worth noting that quantities $\Lambda^{(n)}(\mathbf{r}, \mathbf{r}_k, T_\Lambda; \sigma), n = 0, 1, \ldots, N_t$ are time-invariant, and for a given conductivity model are calculated only once, then stored and used when the calculation of $\mathbf{E}_h(\mathbf{r}, t; \sigma)$ is required.

It is also important to note that the "memory" T_Λ can be taken as short as 15 min (at least for Fennoscandia – the region we have selected to validate the presented approach). Namely, a small value for T_Λ allows us to calculate $\mathbf{E}_h(\mathbf{r}, t; \sigma)$ in real time, provided long-term continuous observations of the magnetic field, $\mathbf{B}_h^{\text{obs}}$ are available at multiple locations. Further justification of T_Λ smallness is presented in the following two sections.

Ideally, Λ should relate the electric field with the magnetic field measured at as large as possible number of sites. However, there are usually gaps in the magnetic field data. At the same time, to apply the presented methodology, one needs to use continuous time series of magnetic field during the interval $[t_i - T_\Lambda, t_i]$ to compute $\mathbf{E}_h(\mathbf{r}, t_i; \sigma)$. Thus one has to choose observatories accordingly to continuous data availability. However, one can use different (precomputed) sets of Λ for different time instances t_i. Combining this option with the short T_Λ means that the number of sites with magnetic field observations in use is always large enough to implement the proposed approach.

The final remark of this section is that if the spatial modes are just two polarizations of vertically indenting plane wave, then Λ degenerates to intersite impedance Z; cf. Section 2.2 of (Marshalko et al., 2023).

3 Results

3.1 3-D conductivity model

One of the critical components required for as realistic as feasible GEF modeling is a trustworthy conductivity model of the Earth's subsurface in the region of interest. The conductivity model of Fennoscandia we adopt comprises a 3-D part (upper 60 km below the surface of the Earth) and the 1-D part underneath taken as a corresponding piece (deeper than 60 km) of the 1-D profile from (Kuvshinov et al., 2021). As for the 3-D part, it is based on the SMAP model (Korja et al., 2002), covers the area of 2550$\times$ 2550 km^2 and consists of three layers of laterally variable conductivity of 10, 20, and 30 km thicknesses. The lateral discretization of the model is 512$\times$512 cells, meaning that cells' size is about 5$\times$5 km^2. Note that this model (of the same discretization) was also used in (Marshalko et al., 2021; Kruglyakov, Kuvshinov, & Marshalko, 2022; Marshalko et al., 2023). The interested reader can find details on the conductivity distribution in the model, for example, in (Kruglyakov, Kuvshinov, & Marshalko, 2022), cf. their Figure 7. Note also that for T_Λ calculations only observatories located in the area covered by this model are used, i.e. not all IMAGE observatories.

3.2 Deriving spatial modes

As mentioned in the Introduction, spatial modes $\mathbf{j}_l(\mathbf{r})$ are obtained using the SECS method and their derivation involves the following two steps (Kruglyakov, Kuvshinov, & Marshalko, 2022):

1. Spherical Elementary Current Systems (SECS) method (Vanhamäki & Juusola, 2020) is applied to 29–31 October 2003 (Halloween storm) ten-second IMAGE magnetic field data to separate the inducing and induced current systems that are assumed to flow 90 km above the Earth's surface and 1 m below the Earth's surface, correspondingly. The data from all 26 magnetometers were used to perform the SECS analysis. The locations of IMAGE magnetometers in use are demonstrated in Figure 1. Note that IMAGE data for this 72-hour time interval contain several gaps; linear interpolation was applied to fill these gaps.

2. The time-domain PCA is applied to the SECS-recovered inducing source resulting in the desired $\mathbf{j}_l(\mathbf{r}), l = 1, 2, ..., L$. With $L = 34$, we described 99.9% of the inducing source variability.

It is relevant to mention that later in the paper, we analyze the data from the Halloween storm and other space weather events. One can argue that $\mathbf{j}_l$ obtained for a specific event could be non-adequate for other events. Kruglyakov, Kuvshinov, and Marshalko (2022) addressed this question and demonstrated that irrespective of the event (which corresponds to sources of different geometry), the spatial structure of these sources is well approximated by a finite number of $\mathbf{j}_l$ obtained from the analysis of some specific event (in our case the Halloween storm). The prerequisite to getting an adequate set of $\mathbf{j}_l$ is that the event for their estimation should be long enough and sufficiently energetically large and spatially complex.

3.3 Comparing modeled and observed GEF

Even though there are multiple locations in Fennoscandia where continuous ground electric field measurements were performed for relatively long time intervals (from weeks to months), our analysis of the available data reveals that most of the GEF observations were conducted during periods of relatively quiet geomagnetic activity. Note that the potentially hazardous GIC are flowing in the technological systems during geomagnetic disturbances like geomagnetic storms and magnetospheric substorms, making such space weather events of particular interest in the context of this study. Fortunately, continuous (one-second) GEF measurements performed in August 2005 – June 2006 at 8 of 13 sites around Joensuu, Finland, in the framework of Electromagnetic Mini Array (EMMA) Project (Smirnov et al., 2006) have successfully recorded prominent space weather event – magnetospheric substorm of 11 September 2005; during this event, amplitudes of the observed GEF in the region exceeded 2000 mV/km. We compare modeled and measured time series of the GEF during this event at two sites (denoted below as M02 and M05) where the largest GEF amplitudes were observed and where the data quality – in terms of absence of gaps, jumps, and electrodes' drift – was the highest. The comparison is performed for the time interval from 05:15 UT to 6:15 UT. This interval includes a 30-min long event and 15-min long quiet periods before and after the event. During this time interval, 16 IMAGE observation sites delivered uninterrupted magnetic field recordings, and thus, only the data from these sites were used to calculate the GEF using Equation (6). Figure 2 shows the location of these IMAGE sites (blue circles) and two sites (red circles) with GEF recordings selected for comparison of the observed and modeled GEF. Since GEF measurements were performed in geomagnetic coordinates, we decided to compare observed and modeled GEF components in this coordinate system. Thus, in this section, the x- and y-components of the GEF are geomagnetic North and East compo-

nents, respectively. Besides, experimental 1-sec time series of the GEF were re-sampled to a 10-sec time series to make them compatible with IMAGE magnetic field data.

It is important to note here that depending on location, the modeled GEF might still over- or underestimate the amplitudes of the actual GEF. This is due to galvanic effects, i.e. the build-up of electric charges along local near-surface heterogeneities (Jiracek, 1990) that cannot be included in the model. Galvanic effects are commonly accounted for with a 2×2 real-valued time-independent – unique for each location – distortion matrix, D, which linearly relates observed $\mathbf{E}_h^{\rm obs}$ and modeled $\mathbf{E}_h^{\rm mod}$ electric fields as (Püthe et al., 2014)

$$\mathbf{E}_h^{\rm obs}(\mathbf{r},t) = D(\mathbf{r})\mathbf{E}_h^{\rm mod}(\mathbf{r},t), \qquad D(\mathbf{r}) = \begin{pmatrix} D_{xx} & D_{xy} \\ D_{yx} & D_{yy} \end{pmatrix}. \tag{8}$$

Having observed and calculated GEF at many time instants and bearing in mind that D is time-independent, we can form highly over-determined SLE given by Equation (8) to estimate elements of D using the least-square method. Specifically, these elements are estimated row-wise as the solutions of the following two SLEs

$$D_{xx}E_x^{\rm mod}(t_i) + D_{xy}E_y^{\rm mod}(t_i) = E_x^{\rm obs}(t_i), \tag{9}$$

and

$$D_{yx}E_x^{\rm mod}(t_i) + D_{yy}E_y^{\rm mod}(t_i) = E_y^{\rm obs}(t_i), \tag{10}$$

where t_i runs multiple (K) time instants. Note that the dependence of all quantities in Equations (9) and (10) on $\mathbf{r}$ is omitted but implied. To make the comparison as fair as possible, we calculated distortion matrices using the data not from the time interval where we compare the results (05:15 – 06:15 September 11) but using the data far before the event, specifically, namely the data from one (whole; September 9) day, giving $K = 24\times 3600/10 = 8640$ equations to estimate respective two elements.

As stated in the previous section, the memory T_Λ can be taken as short as 15 min in Equation (6). To explore whether this is the case, we performed GEF calculations taking T_Λ as 15, 30, 60 and 90 min. Figures 3 and 4 compare observed and (corrected for the distortion) modeled E_x and E_y, respectively, at sites M02 and M05 for different values of T_Λ. Note that the corrected modeled GEF are calculated by reusing Equation (8), i.e., as

$$\mathbf{E}_h^{\rm mod,corr}(\mathbf{r},t) = D(\mathbf{r})\mathbf{E}_h^{\rm mod}(\mathbf{r},t), \tag{11}$$

where elements of D are obtained from the solution of the SLEs (9) and (10). As is seen, the modeled results for all values of T_Λ are indistinguishably similar, meaning that T_Λ can be taken as 15 min. Tables 1 and 2 confirm this inference more quantitatively by showing correlation coefficients and coefficients of determination at sites M02 and M05, respectively, for the considered 1-hour time interval. One can see that both quantities practically do not differ with respect to the value of T_Λ.

What is also noticeable from the tables is that the agreement between experimental and modeled GEF (in terms of both correlation coefficients and coefficients of determination) is better in the E_y component. This is most probably because the ionospheric current (source) flows predominantly in the y direction, making GEF modeling in this direction more accurate. Returning to Figures 3 and 4, we also observe that the experimental GEF at selected sites separated by only 21 km significantly differ, more considerably than the modeled GEF. The most probable reason for this is the existence of local 3-D conductivity heterogeneities in this region which are not accounted for in the available 3-D conductivity model of the region.

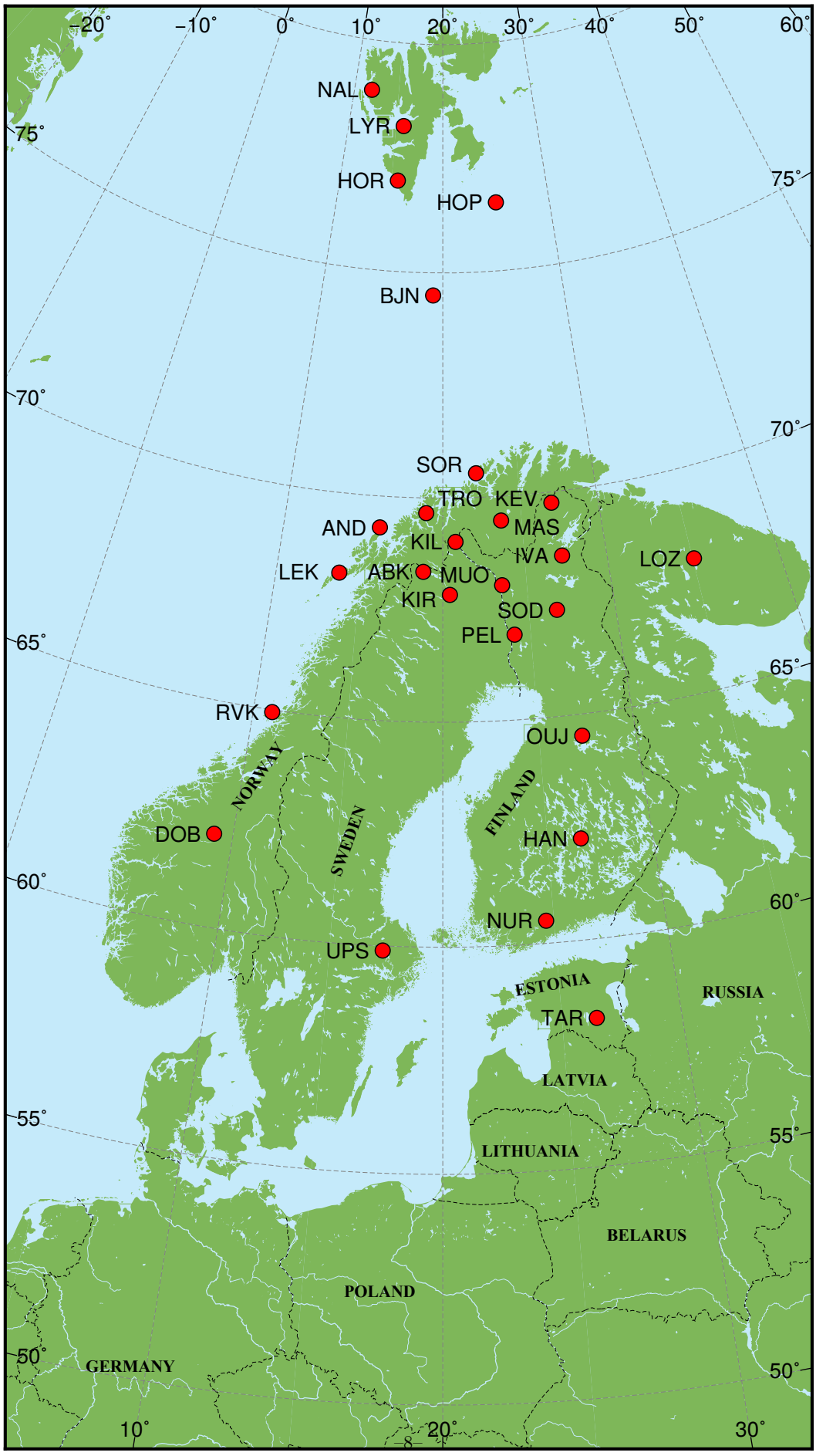

Figure 1. Location of IMAGE observatories with available data for 29 – 31 October 2003.

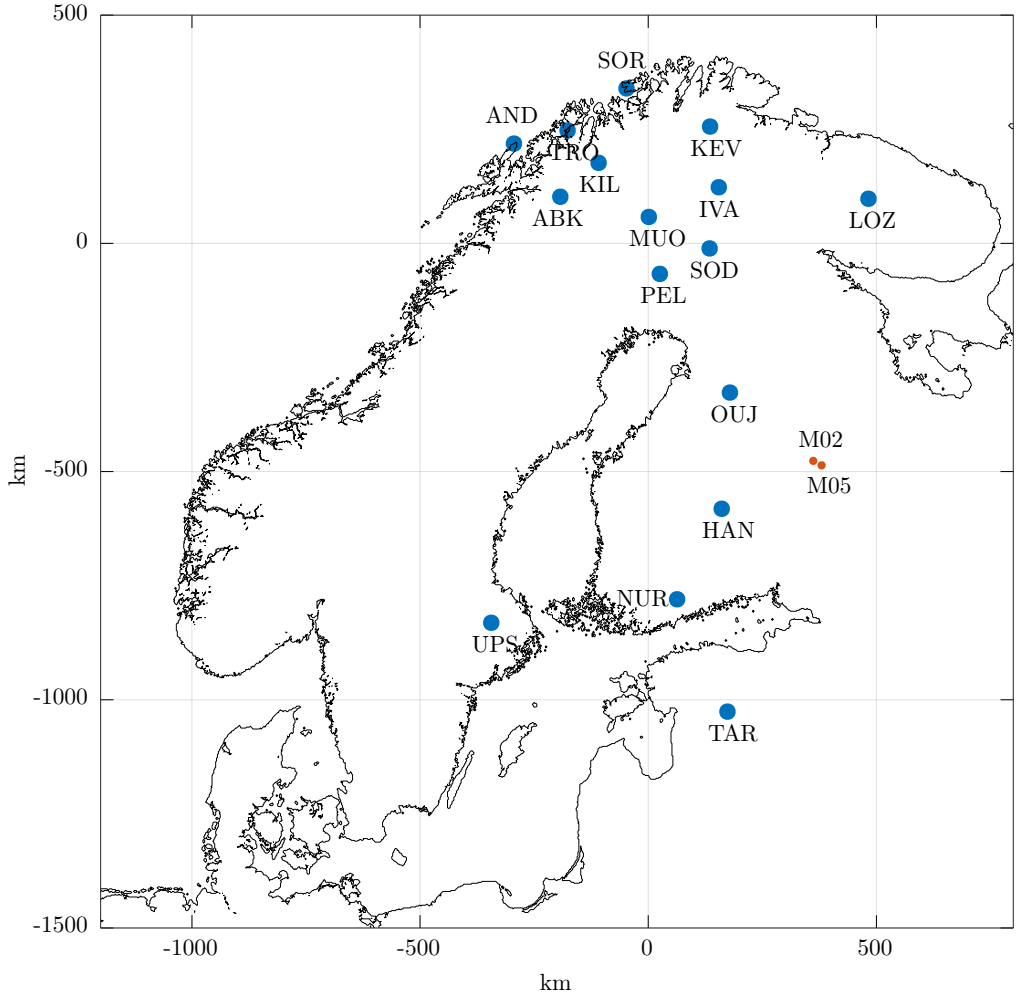

Figure 2. Location of IMAGE sites (blue-filled circles) used for GEF simulation (see Equation 6). Red circles – the location of sites where the GEF was measured and used for comparison with the simulated GEF.

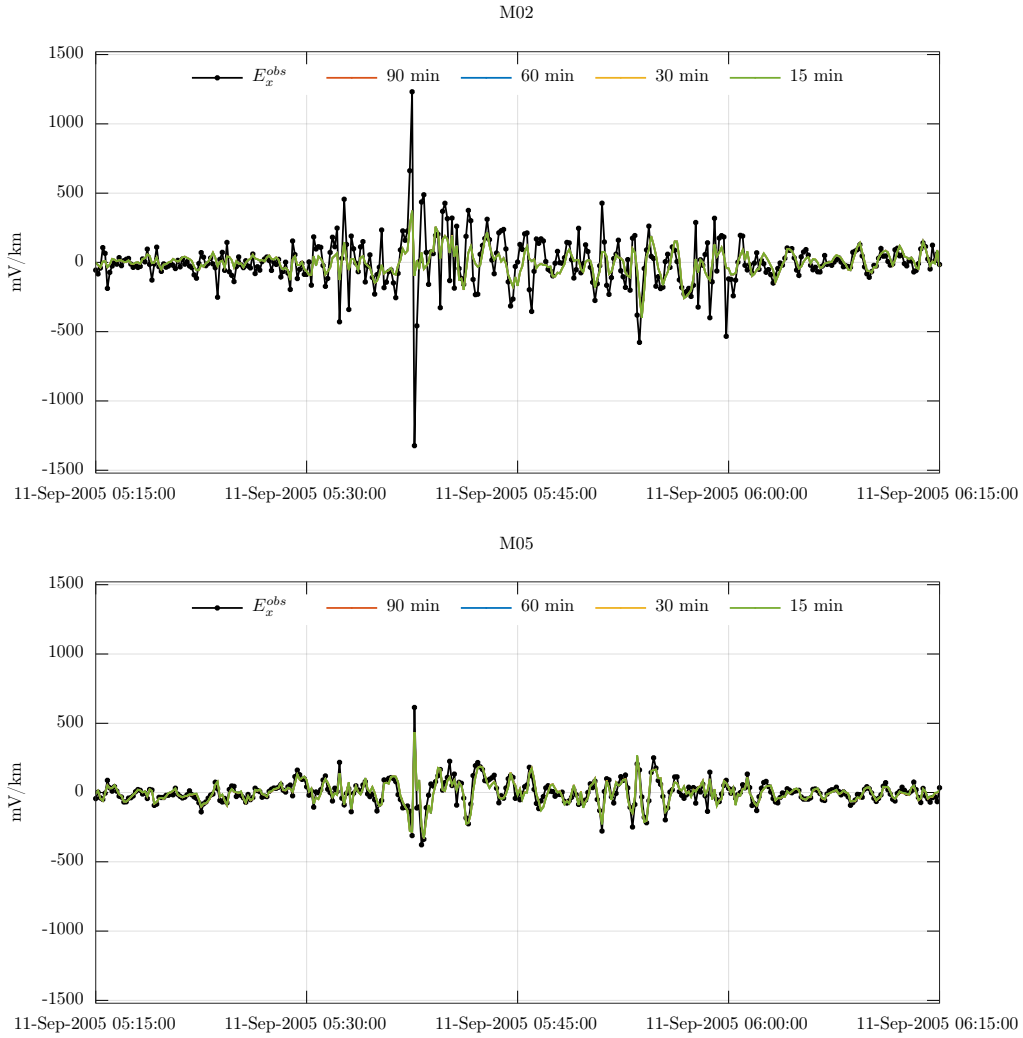

Figure 3. Comparison of the (geomagnetic) northward component of observed and modeled GEF at M02 and M05 sites for different values of T_Λ.

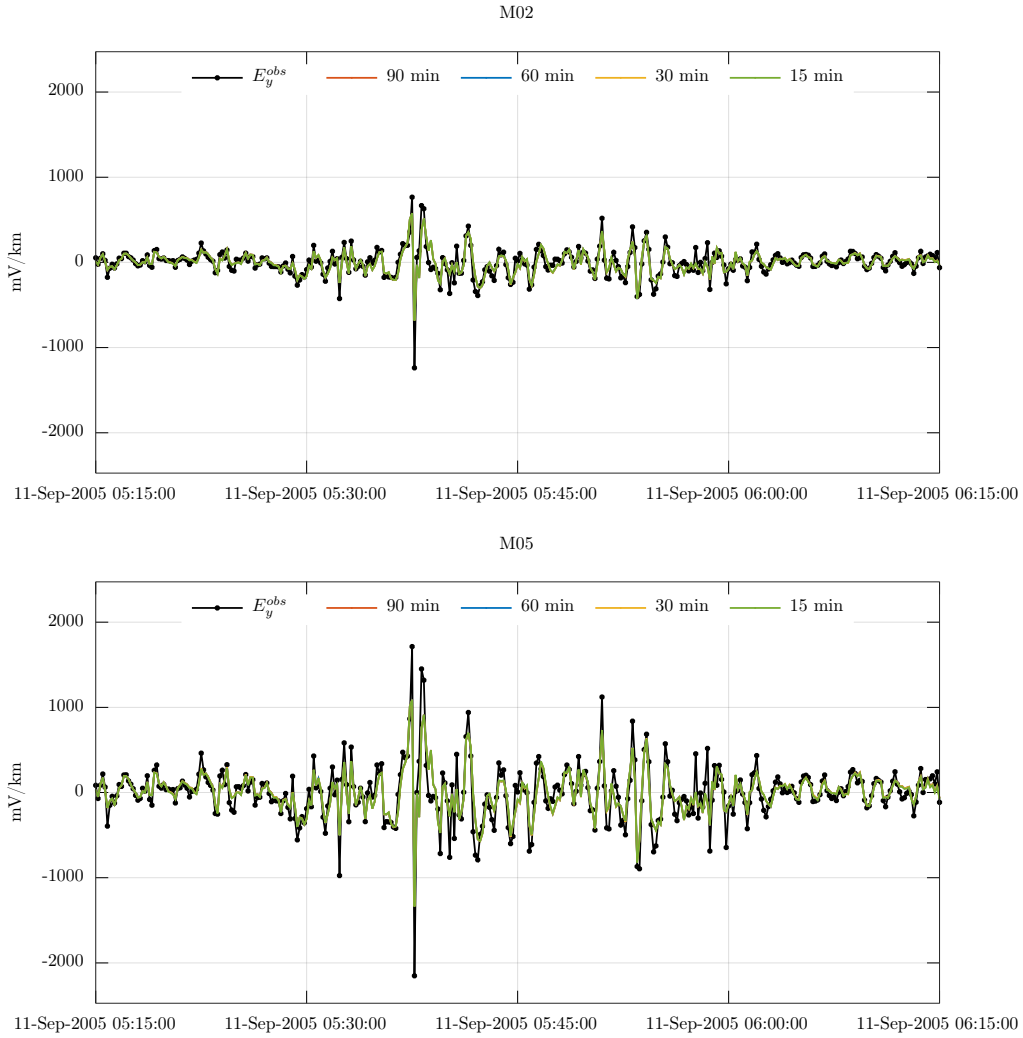

Figure 4. Comparison of the (geomagnetic) eastward component of observed and modeled GEF at M02 and M05 sites for different values of T_Λ.

Table 1. The agreement between modeled and observed GEF at site M02 in terms of correlation coefficients and coefficients of determination.

T_Λ, min	Corr for E_x	Corr for E_y	R^2 for E_x	R^2 for E_y
15	0.635	0.881	0.371	0.768
30	0.633	0.881	0.370	0.767
60	0.632	0.881	0.369	0.767
90	0.632	0.880	0.369	0.766

Table 2. The agreement between modeled and observed GEF at site M05 in terms of correlation coefficients and coefficients of determination.

T_Λ, min	Corr for E_x	Corr for E_y	R^2 for E_x	R^2 for E_y
15	0.882	0.891	0.777	0.767
30	0.882	0.890	0.778	0.766
60	0.882	0.890	0.778	0.766
90	0.882	0.890	0.778	0.766

4 Comparing observed and modeled GIC

The conventional approach to simulate GIC in the pipelines is based on the following linear model (Boteler, 2013; Boteler & Pirjola, 2014))

$$GIC(\mathbf{r},t) = \sum_{i=1}^{M} \left[a_i(\mathbf{r}) E_x(\mathbf{r}_i,t) + b_i(\mathbf{r}) E_y(\mathbf{r}_i,t) \right], \tag{12}$$

where M is the number of pipeline nodes and ends, $\mathbf{r}_i$ – coordinates of their location, and $\mathbf{r}$ is the coordinate of the pipeline point where GIC is recorded. Note that coefficients a_i and b_i are time-independent, but depend on pipeline physical parameters. In case when the conductivity distribution and the source are both laterally uniform, Equation (12) degenerates to

$$GIC(\mathbf{r},t) = a(\mathbf{r}) E_x(\mathbf{r},t) + b(\mathbf{r}) E_y(\mathbf{r},t). \tag{13}$$

The formula (13) has been used in many studies (for example, Pulkkinen et al. (2001); Trichtchenko and Boteler (2002); Wawrzaszek et al. (2023)), but due to the obvious lateral nonuniformity of the conductivity distribution and the source in the region under investigation, we use Equation (12) to calculate GIC.

Having observed GIC and calculated GEF at many time instants, and bearing in mind that coefficients a_i and b_i are time-independent, we can form – as for elements of matrix D discussed in the previous section – highly over-determined SLE given by Equation (12) to estimate coefficients using the least-squares method. Precisely, these coefficients are calculated as the solution of the following SLE

$$a_1 E_x^{\mathrm{mod}}(\mathbf{r}_1,t_i) + b_1 E_y^{\mathrm{mod}}(\mathbf{r}_1,t_i) + \ldots + a_M E_x^{\mathrm{mod}}(\mathbf{r}_M,t_i) + b_M E_y^{\mathrm{mod}}(\mathbf{r}_M,t_i) = GIC^{\mathrm{obs}}(t_i), \tag{14}$$

where t_i runs multiple (K) time instants. Here we omit the dependence of the coefficients and $\mathrm{GIC}^{\mathrm{obs}}$ on $\mathbf{r}$ because we have GIC's recordings only at one (Mäntsälä; MAN) point. Figure 5 shows the general geometry of the pipeline (gray lines) and location of 18 pipeline's nodes and ends (gold diamonds). The geometry of the pipeline is based on models presented in (Pulkkinen et al., 2001) and (Dimmock et al., 2019).

GIC measurements at the Mäntsälä point have been performed continuously since 1999; thus, we had an opportunity to compare observed and modeled GIC for a number of events.

Table 3. The agreement between modeled and observed GIC in terms of correlation coefficients and coefficients of determination for different events (substorms).

Substorms	Correlation	R^2
15 July – 16 July 2000	0.909	0.826
05 November – 06 November 2001	0.895	0.782
29 October – 1 November 2003	0.936	0.871

We have chosen events that happened in 2000, 2001, and 2003 years. It should be noted that the approach we use to determine coefficients a_i and b_i is implicitly based an assumption that the configuration of the pipeline system was the same during the events in study. Concerning the relatively short period of 2000 – 2003, no major modifications of the pipeline network were made. However, the present pipeline system is more extensive than in the beginning of 2000's.

Note also that from 2005 the quality of GIC measurements degraded; this is why we considered earlier years' events. Also, note that the modeled GIC are calculated by reusing Equation (12)

$$GIC^{\rm mod}(t) = \sum_{i=1}^{M} \left[a_i E_x^{\rm mod}(\mathbf{r}_i, t) + b_i E_y^{\rm mod}(\mathbf{r}_i, t) \right], \tag{15}$$

where a_i and b_i are obtained from the solution of the SLE (14). GEF in Equation (15) were calculated using $T_\Lambda = 15$ min; our model experiments (not shown in the paper) with larger T_Λ reveal a negligible difference in the modeled GIC. As in the case of the GEF comparison discussed in the previous section, we estimated a_i and b_i using GIC data not from the time interval where we compare the results but using continuous data for 27 – 28 October 2003, giving $K = 2 \times 24 \times 3600/10 = 17280$ equations to estimate respective $2 \times M = 36$ coefficients.

Top two panels in Figures 6 – 8 demonstrate time series of observed and modeled GIC for two 3-hour time intervals of corresponding years/months when large fluctuations of GIC were detected. As one can see, the agreement between observed and modeled GIC is remarkably good. The bottom right panels in the figures demonstrate the agreement differently. It shows cross-plots of the observed and modeled GIC. Ideally, the observed and modeled GIC would lie in a straight line, and this is indeed the case. Note that the bottom left panel shows IMAGE observatories, the data from which were used to calculate the GEF using Equation (6).

Finally, Table 3 demonstrates the agreement in a more quantitative way by presenting correlation coefficients and coefficients of determination for the considered events. One can see that both coefficients are close to 1, irrespective of the event. Interestingly, the agreement in GIC is better than in GEF (see previous section). We attribute better agreement in GIC to a smoothing effect of summation (see Equation (15)) which effectively suppresses the potential inaccuracy of modeled GEF at considered nodes and ends.

5 Conclusions

This paper presents a novel approach to the GEF calculation in real time. The approach makes it possible to take into account the 3-D Earth's conductivity distribution in the region and lateral variability of the source. It works with spatial modes describing the spatial structure of the source and exploits the multi-site (MS) transfer function

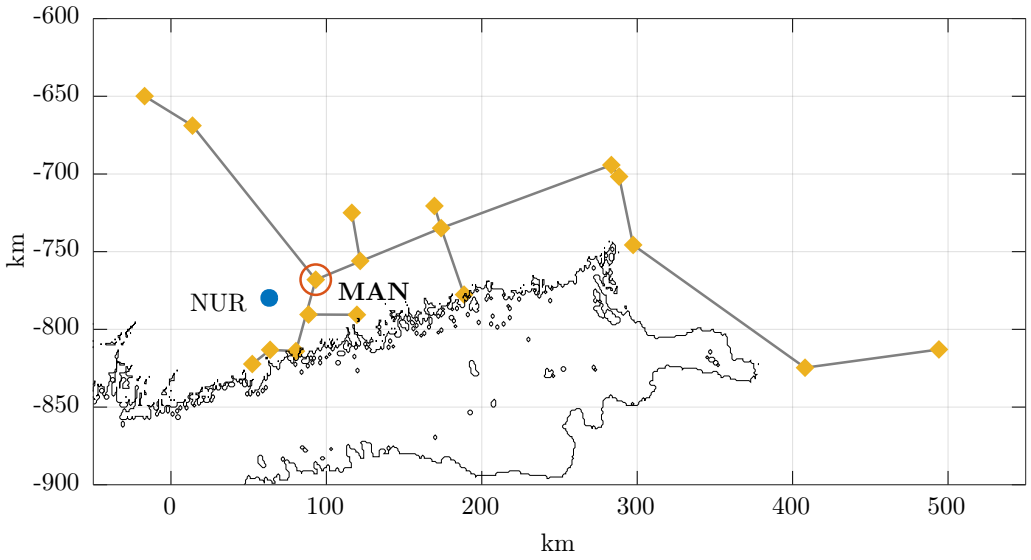

Figure 5. Geometry of the pipeline (grey lines) and location of 18 pipeline's nodes and ends (gold diamonds); Mäntsälä (MAN) natural gas pipeline recording point (open red circle). For reference, the location of the IMAGE observatory, Nurmijärvi (NUR; blue-filled circle) is shown.

(TF) concept where MS TF relate the GEF at any location with horizontal magnetic field at (fixed) multiple locations.

Using Fennoscandia as an example region and the SECS method to derive the spatial modes, we compared the observed time series of the GEF and GIC available in the region with those simulated using the proposed approach. Good agreement between observed and modeled results validates the methodology. Notably, in contrast to the previous study (Marshalko et al., 2023), where GIC was calculated using the GEF at the pipeline node where GIC is measured, in this paper, we considered a more realistic scenario when GIC is calculated using simulated GEF at multiple nodes of the actual pipeline grid.

While the simulations of GICs in this paper are mainly done for validation purposes, the presented approach opens an avenue to derive a GIC activity indicator. Combining (6) and (15) one can estimate GIC in real time. Moreover, as demonstrated in this paper, the estimated GIC values correspond very accurately to the true recordings for a particular period when the conductor network can be assumed to be unchanged. Outside of this period, the resulting GIC provides a meaningful proxy. Although it may not any more give the true current, it can still be compared to other events in a relative sense. For example, in our case, we could use the Halloween storm as a benchmark. Thus this method has an immediate potential to be implemented as an operative product for space weather services.

The prerequisite for the method's application is continuous magnetic field measurements at multiple locations, as in Fennoscandia. North America and China (with existing networks of magnetic field observations), or/and New Zealand (with the network of variometers is being established now) are regions where the proposed method is worth trying.

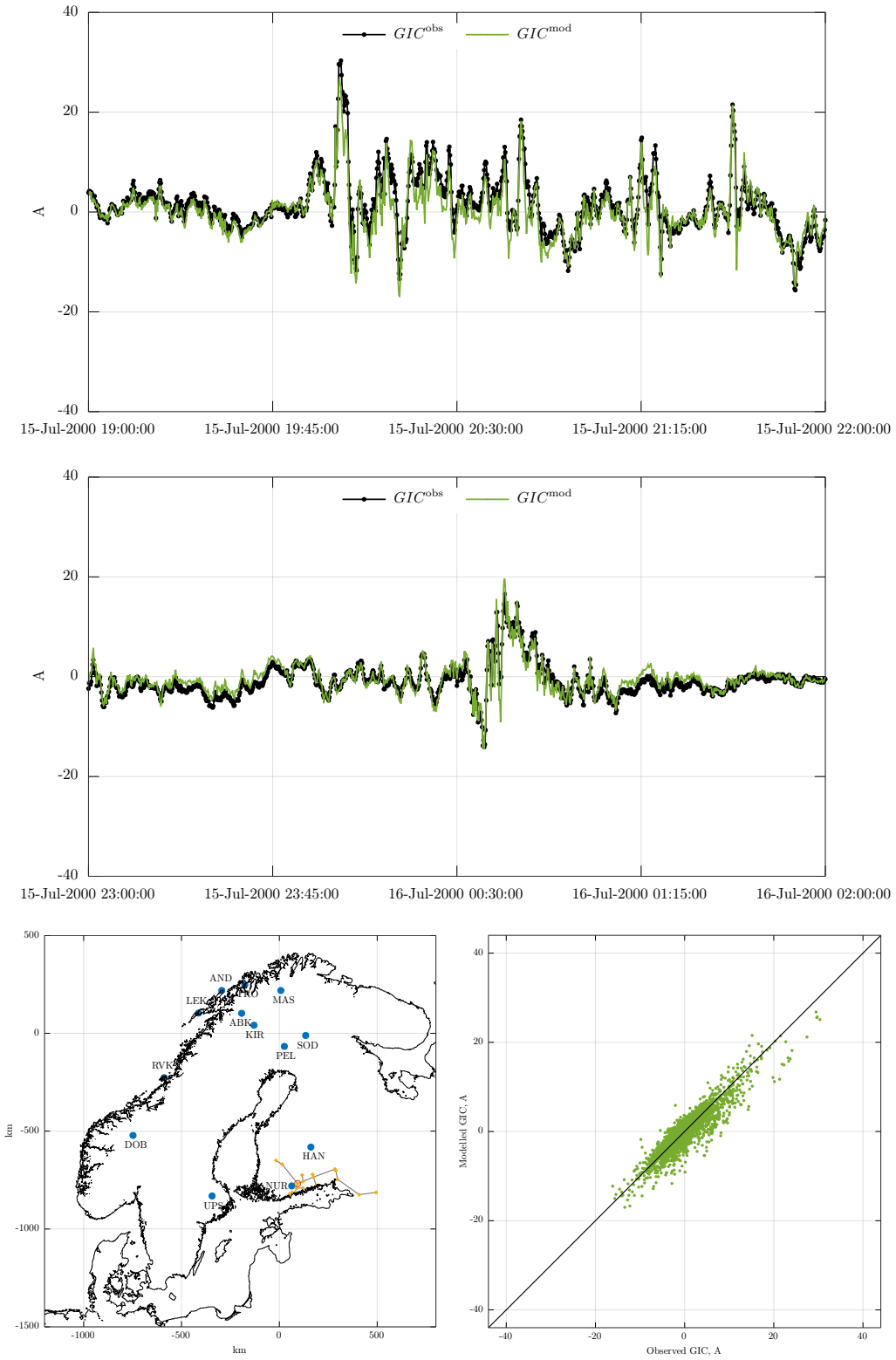

Figure 6. Substorms of 15/16 July 2000. Top two panels: comparison of observed and modeled GIC for two 3-hour time intervals. Bottom left panel: location of 13 IMAGE sites (blue-filled circles) used for the GEF simulation. Bottom right panel: cross-plots of observed and modeled GIC (cross-plots are demonstrated for the 2-day time interval: July 15 – 16 2000).

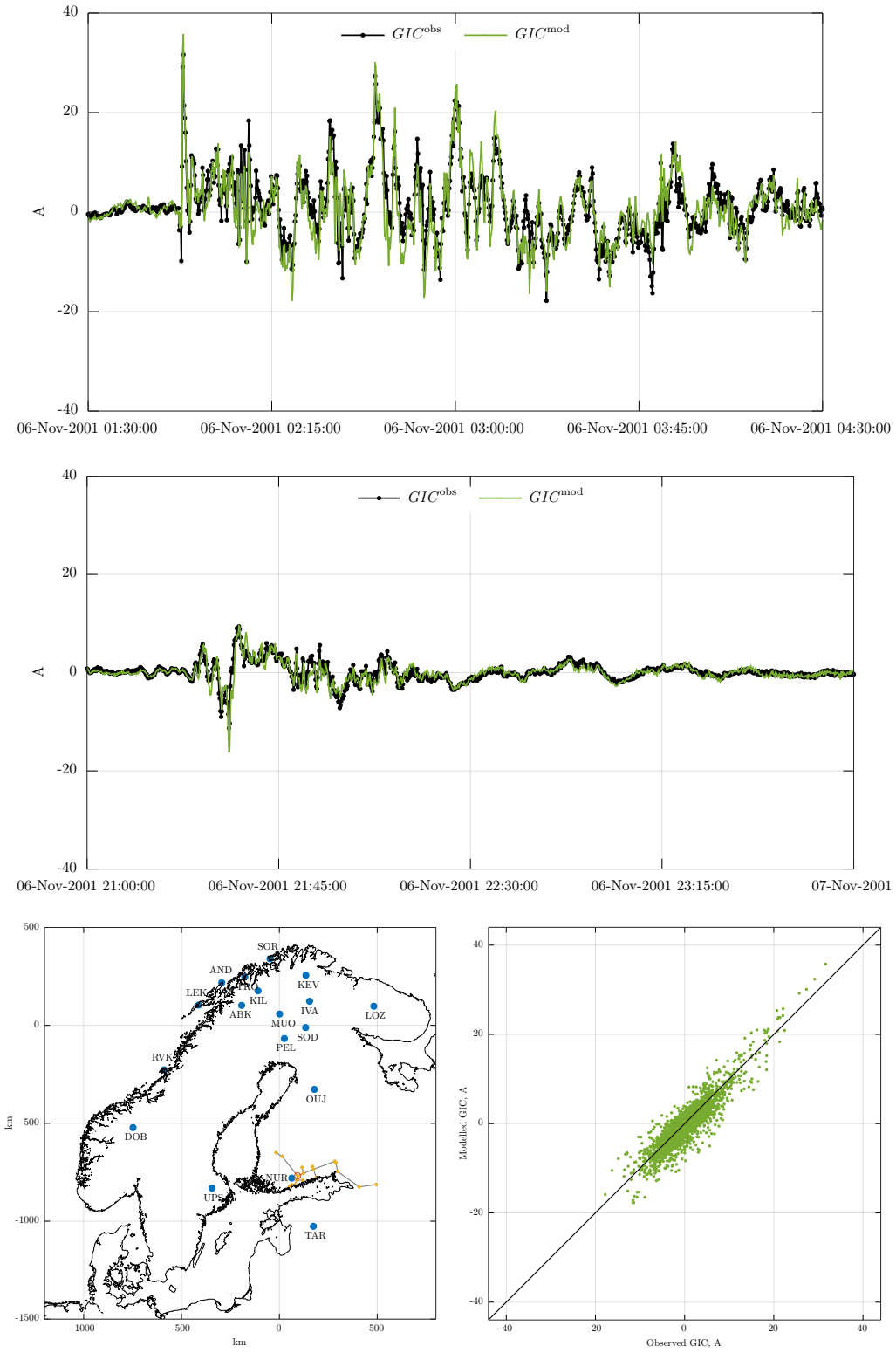

Figure 7. Substorms of 6 November 2001. Top two panels: comparison of observed and modeled GIC for two 3-hour time intervals. Bottom left panel: location of 18 IMAGE sites (blue-filled circles) used for the GEF simulation. Bottom right panel: cross-plots of observed and modeled GIC (cross-plots are demonstrated for the 2-day time interval: November 5 – 6 2001).

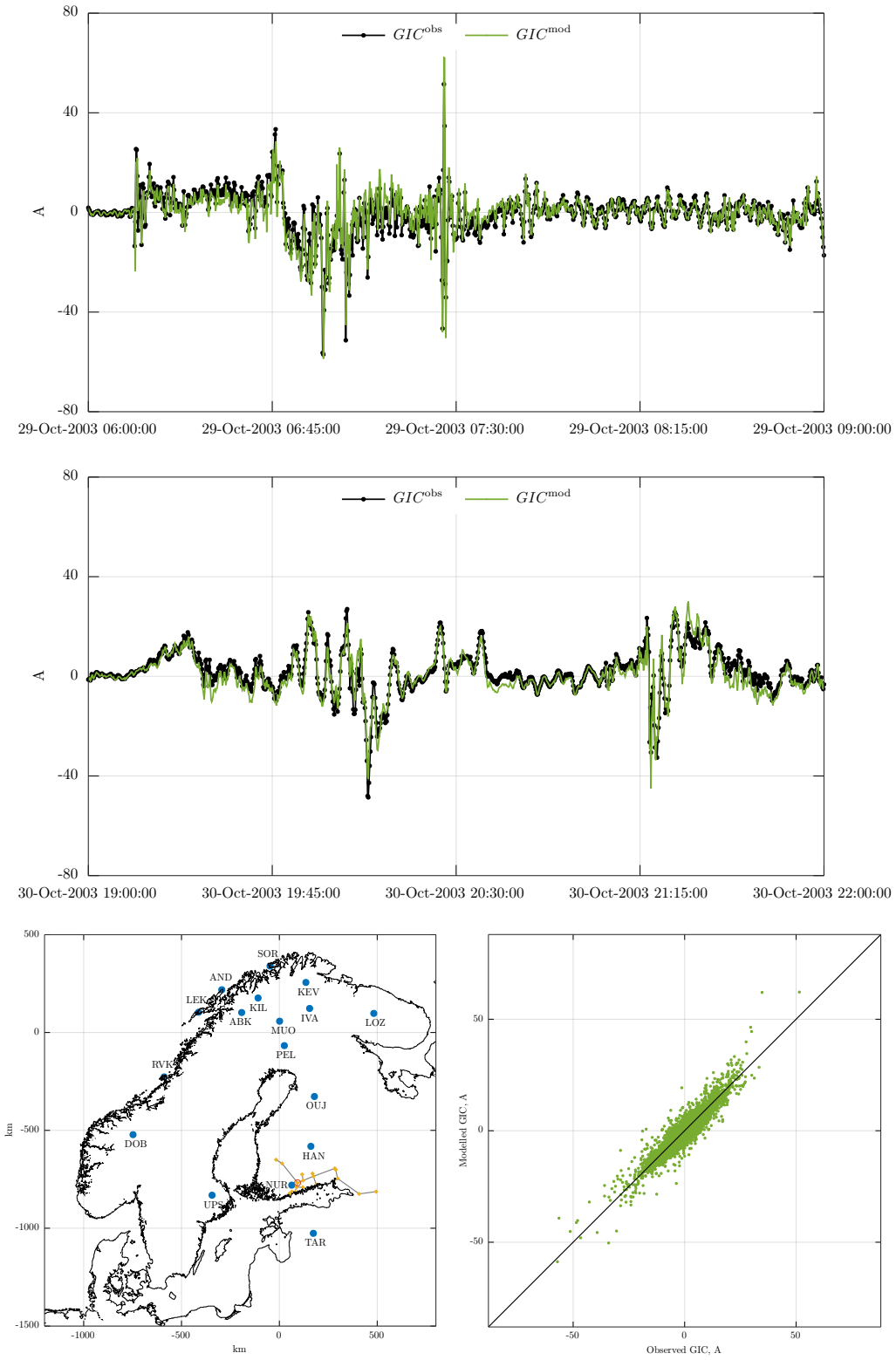

Figure 8. Substorms of 29/30 October 2003. Top two panels: comparison of observed and modeled GIC for two 3-hour time intervals. Bottom left panel: location of 17 IMAGE sites (blue-filled circles) used for the GEF simulation. Bottom right panel: cross-plots of observed and modeled GIC (cross-plots are demonstrated for the 3-day time interval: October 29 – November 1 2003).

It is worth noting that while comparing measured and simulated GEF at two selected sites separated by only 21 km, we observe that experimental GEF at these sites differ more significantly than the modeled GEF. Bearing in mind that the inducing source (equivalent ionospheric current) is relatively (spatially) smooth, the most probable reason for substantial lateral variability of the experimental GEF is local sharp lateral gradients of the subsurface conductivity not accounted for in the used 3-D conductivity model of the region. This prompts building a new – more accurate and detailed – 3-D conductivity model of Fennoscandia via a multi-scale 3-D inversion (using new modern inverse solvers) of both old data (on which SMAP model was based) and a large amount of new MT data collected in the region in the framework of various MT projects.

Finally, we have to mention that the proposed concept of multi-site transfer functions can be easily adapted to another space weather related problem – accounting for the geomagnetic disturbances during offshore directional drilling in northern seas (like offshore of Alaska, Norway, British Isles, and North Russia), where magnetic field variations are routinely recorded at multiple adjacent land-based locations. In this scenario, MS TF will relate magnetic field variations at sea bottom with those at multiple land-based sites.

6 Open Research

The SMAP model (Korja et al., 2002) is available at the European Plate Observing System (EPOS) portal via EPOS (2019) (stored in JSON format and compressed with bzip2) under CC BY-NC 4.0. PGIEM2G 3-D EM forward modeling code is available at Kruglyakov (2022) under GPLv2. GIC data are available at the website of the Space and Earth Observation Centre of the Finnish Meteorological Institute (FMI) via FMI (2023) under CC BY 4.0.

Acknowledgments
MK was supported by the New Zealand Ministry of Business, Innovation, & Employment through Endeavour Fund Research Programme contract UOOX2002. AK and MK were also partially supported in the framework of Swarm DISC activities, funded by ESA contract no. 4000109587, with support from EO Science for Society. EM and AV were supported by grants 339329 from the Academy of Finland. We thank the institutes that maintain the IMAGE Magnetometer Array: Tromsø Geophysical Observatory of UiT, the Arctic University of Norway (Norway), Finnish Meteorological Institute (Finland), Institute of Geophysics Polish Academy of Sciences (Poland), GFZ German Research Center for Geosciences (Germany), Geological Survey of Sweden (Sweden), Swedish Institute of Space Physics (Sweden), Sodankylä Geophysical Observatory of the University of Oulu (Finland), and Polar Geophysical Institute (Russia). We acknowledge Gasum Oy for long-term collaboration in GIC studies of the Finnish natural gas pipeline.

References

Bailey, R., Halbedl, T. S., Schattauer, I., Achleitner, G., & Leonhardt, R. (2018). Validating GIC models with measurements in Austria: Evaluation of accuracy and sensitivity to input parameters. *Space Weather*, *16*(7), 887–902. doi: 10.1029/2018SW001842

Beggan, C. D. (2015). Sensitivity of geomagnetically induced currents to varying auroral electrojet and conductivity models. *Earth Planets Space*, *67*(24). doi: 10.1186/s40623-014-0168-9

Beggan, C. D., Richardson, G. S., Baillie, O., Hübert, J., & Thomson, A. W. P. (2021). Geolectric field measurement, modelling and validation during geomagnetic storms in the UK. *J. Space Weather Space Clim.*, *11*, 37.

https://doi.org/10.1051/swsc/2021022 doi: 10.1051/swsc/2021022

Boteler, D. H. (2013, 01). A new versatile method for modelling geomagnetic induction in pipelines. *Geophysical Journal International*, *193*(1), 98-109. https://doi.org/10.1093/gji/ggs113 doi: 10.1093/gji/ggs113

Boteler, D. H., & Pirjola, R. J. (2014). Comparison of methods for modelling geomagnetically induced currents. *Annales Geophysicae*, *32*(9), 1177–1187. https://angeo.copernicus.org/articles/32/1177/2014/ doi: 10.5194/angeo-32-1177-2014

Campanyà, J., Gallagher, P. T., Blake, S. P., Gibbs, M., Jackson, D., Beggan, C. D., ... Hogg, C. (2019). Modeling geoelectric fields in ireland and the uk for space weather applications. *Space Weather*, *17*(2), 216-237. https://agupubs.onlinelibrary.wiley.com/doi/abs/10.1029/2018SW001999 doi: https://doi.org/10.1029/2018SW001999

Dimmock, A. P., Rosenqvist, L., Hall, J.-O., Viljanen, A., Yordanova, E., Honkonen, I., ... Sjöberg, E. C. (2019). The GIC and geomagnetic response over Fennoscandia to the 7-8 September 2017 geomagnetic storm. *Space Weather*, *17*(7), 989–1010. doi: 10.1029/2018SW002132

Divett, T., Ingham, M., Beggan, C. D., Richardson, G. S., Rodger, C. J., Thomson, A. W. P., & Dalzell, M. (2017). Modeling geoelectric fields and geomagnetically induced currents around New Zealand to explore GIC in the South Island's electrical transmission network. *Space Weather*, *15*(10), 1396–1412. doi: 10.1002/2017SW001697

Divett, T., Mac Manus, D. H., Richardson, G. S., Beggan, C. D., Rodger, C. J., Ingham, M., ... Obana, Y. (2020). Geomagnetically induced current model validation from New Zealand's South Island. *Space Weather*, *18*(8), e2020SW002494. doi: 10.1029/2020SW002494

EPOS. (2019). *Dataset for "Crustal conductivity in Fennoscandia – a compilation of a database on crustal conductance in the Fennoscandian Shield", Korja et al., 2002, Earth, Planets and Space* [Dataset]. European Plate Observing System (EPOS). https://mt.research.ltu.se/MT/BEAR/1998/BEAR_3D.mod.json

FMI. (2023). *GIC recordings in the Finnish natural gas pipeline - ASCII files* [Dataset]. Finnish Meteorological Institute (FMI). https://space.fmi.fi/gic/man_ascii/man.php

Honkonen, I., Kuvshinov, A., Rastätter, L., & Pulkkinen, A. (2018). Predicting global ground geoelectric field with coupled geospace and three-dimensional geomagnetic induction models. *Space Weather*, *16*(8), 1028–1041. doi: 10.1029/2018SW001859

Jiracek, G. R. (1990). Near-surface and topographic distortions in electromagnetic induction. *Surv. Geophys.*, *11*, 163-203.

Kelbert, A., Balch, C., Pulkkinen, A., Egbert, G., Love, J., Rigler, J., & Fujii, I. (2017). Methodology for time-domain estimation of storm time geoelectric fields using the 3-D magnetotelluric response tensors. *Space Weather*, *15*(7), 874–894. doi: doi:10.1002/2017SW001594

Korja, T., Engels, M., Zhamaletdinov, A. A., Kovtun, A. A., Palshin, N. A., Smirnov, M. Y., ... BEAR Working Group (2002). Crustal conductivity in Fennoscandia – a compilation of a database on crustal conductance in the Fennoscandian Shield. *Earth, Planets and Space*, *54*, 535–558. doi: 10.1186/BF03353044

Kruglyakov, M. (2022). *PGIEM2G* [Software]. Gitlab. https://gitlab.com/m.kruglyakov/PGIEM2G

Kruglyakov, M., & Kuvshinov, A. (2018). Using high-order polynomial basis in 3-D EM forward modeling based on volume integral equation method. *Geophysical Journal International*, *213*(2), 1387–1401. doi: 10.1093/gji/ggy059

Kruglyakov, M., Kuvshinov, A., & Marshalko, E. (2022). Real-time 3-D modeling of the ground electric field due to space weather events. A concept and its valida-

tion. *Space Weather*, *20*(4), e2021SW002906. doi: 10.1029/2021SW002906

Kruglyakov, M., Kuvshinov, A., & Nair, M. (2022). A proper use of the adjacent land-based observatory magnetic field data to account for the geomagnetic disturbances during offshore directional drilling. *Space Weather*. doi: 10.1029/2022SW003238

Kuvshinov, A., Grayver, A., Tøffner-Clausen, L., & Olsen, N. (2021). Probing 3-D electrical conductivity of the mantle using 6 years of Swarm, CryoSat-2 and observatory magnetic data and exploiting matrix Q-responses approach. *Earth, Planets and Space*, *73*, 67. doi: 10.1186/s40623-020-01341-9

Malone-Leigh, J., Campanyà, J., Gallagher, P. T., Neukirch, M., Hogg, C., & Hodgson, J. (2023). Nowcasting geoelectric fields in Ireland using magnetotelluric transfer functions. *J. Space Weather Space Clim.*, *13*, 6. `https://doi.org/10.1051/swsc/2023004` doi: 10.1051/swsc/2023004

Marshalko, E., Kruglyakov, M., Kuvshinov, A., Juusola, L., Kwagala, N. K., Sokolova, E., & Pilipenko, V. (2021). Comparing three approaches to the inducing source setting for the ground electromagnetic field modeling due to space weather events. *Space Weather*, *19*(2), e2020SW002657. doi: 10.1029/2020SW002657

Marshalko, E., Kruglyakov, M., Kuvshinov, A., Murphy, B. S., Rastätter, L., Ngwira, C., & Pulkkinen, A. (2020). Exploring the influence of lateral conductivity contrasts on the storm time behavior of the ground electric field in the eastern United States. *Space Weather*, *18*(2), 159–195. doi: 10.1029/2019SW002216

Marshalko, E., Kruglyakov, M., Kuvshinov, A., & Viljanen, A. (2023). Rigorous 3-D modeling of the ground electric field in Fennoscandia during the Halloween geomagnetic storm. *Space Weather, revision submitted. Preprint at ESS Open Archive. DOI: 10.22541/essoar.167631318.88816433/v2*.

Marshall, R. A., Dalzell, M., Waters, C. L., Goldthorpe, P., & Smith, E. A. (2012). Geomagnetically induced currents in the new zealand power network. *Space Weather*, *10*(8). `https://agupubs.onlinelibrary.wiley.com/doi/abs/10.1029/2012SW000806` doi: https://doi.org/10.1029/2012SW000806

Marshall, R. A., Wang, L., Paskos, G. A., Olivares-Pulido, G., Van Der Walt, T., Ong, C., ... Yoshikawa, A. (2019). Modeling geomagnetically induced currents in Australian power networks using different conductivity models. *Space Weather*, *17*(5), 727–756. doi: https://doi.org/10.1029/2018SW002047

Nakamura, S., Ebihara, Y., Fujita, S., Goto, T., Yamada, N., Watari, S., & Omura, Y. (2018). Time domain simulation of geomagnetically induced current (GIC) flowing in 500-kv power grid in Japan including a three-dimensional ground inhomogeneity. *Space Weather*, *16*(12), 1946–1959. doi: 10.1029/2018SW002004

Pulkkinen, A., Lindahl, S., Viljanen, A., & Pirjola, R. (2005). Geomagnetic storm of 29–31 October 2003: Geomagnetically induced currents and their relation to problems in the Swedish high-voltage power transmission system. *Space Weather*, *3*(8), S08C03. doi: 0.1029/2004SW000123

Pulkkinen, A., Viljanen, A., Pajunpää, K., & Pirjola, R. (2001). Recordings and occurrence of geomagnetically induced currents in the Finnish natural gas pipeline network. *Journal of Applied Geophysics*, *48*(4), 219–231. doi: 10.1016/S0926-9851(01)00108-2

Püthe, C., Manoj, C., & Kuvshinov, A. (2014). Reproducing electric field observations during magnetic storms by means of rigorous 3-D modelling and distortion matrix co-estimation. *Earth, Planets and Space*, *66*, 162-171.

Rodger, C. J., Mac Manus, D. H., Dalzell, M., Thomson, A. W. P., Clarke, E., Petersen, T., ... Divett, T. (2017). Long-term geomagnetically induced current observations from new zealand: Peak current estimates for extreme geomagnetic storms. *Space Weather*, *15*(11), 1447-1460. `https://`

agupubs.onlinelibrary.wiley.com/doi/abs/10.1002/2017SW001691 doi: https://doi.org/10.1002/2017SW001691

Rosenqvist, L., & Hall, J. O. (2019). Regional 3-D modeling and verification of geomagnetically induced currents in Sweden. *Space Weather*, *17*(1), 27–36. doi: 10.1029/2018SW002084

Smirnov, M., Korja, T., & Pedersen, L. (2006). Electromagnetic Mini Array (EMMA) Project in Fennoscandia Looking into Deep Lithosphere. In *Proceedings of the 7th International Conference: PROBLEMS OF GEOCOSMOS, St. Petersburg.*

Tanskanen, E. I. (2009). A comprehensive high-throughput analysis of substorms observed by IMAGE magnetometer network: Years 1993–2003 examined. *J. Geophys. Res.*, *114*(A5). doi: 10.1029/2008JA013682

Trichtchenko, L., & Boteler, D. H. (2002). Modelling of geomagnetic induction in pipelines. *Annales Geophysicae*, *20*(7), 1063–1072. https://angeo.copernicus.org/articles/20/1063/2002/ doi: 10.5194/angeo-20-1063-2002

Vanhamäki, H., & Juusola, L. (2020). Introduction to Spherical Elementary Current Systems. In M. W. Dunlop & H. Lühr (Eds.), *Ionospheric multi-spacecraft analysis tools: Approaches for deriving ionospheric parameters* (pp. 5–33). Cham: Springer International Publishing. doi: 10.1007/978-3-030-26732-2_2

Viljanen, A., & Pirjola, R. (1994). Geomagnetically induced currents in the Finnish high-voltage power system. A geophysical review. *Surv. Geophys.*, *15*, 383–408. doi: 10.1007/BF00665999

Viljanen, A., Pirjola, R., Wik, M., Ádám, A., Prácser, E., Sakharov, Y., & Katkalov, J. (2012). Continental scale modelling of geomagnetically induced currents. *J. Space Weather Space Clim.*, *2*, A17. doi: 10.1051/swsc/2012017

Viljanen, A., Pulkkinen, A., Pirjola, R., Pajunpää, K., Posio, P., & Koistinen, A. (2006). Recordings of geomagnetically induced currents and a nowcasting service of the Finnish natural gas pipeline system. *Space Weather*, *4*(10). doi: 10.1029/2006SW000234

Wang, L., Lewis, A. M., Ogawa, Y., Jones, W. V., & Costelloe, M. T. (2016). Modeling geomagnetic induction hazards using a 3-D electrical conductivity model of Australia. *Space Weather*, *14*, 1125–1135. doi: 10.1002/2016SW001436

Wawrzaszek, A., Gil, A., Modzelewska, R., Tsurutani, B. T., & Wawrzaszek, R. (2023). Analysis of large geomagnetically induced currents during the 7–8 september 2017 storm: Geoelectric field mapping. *Space Weather*, *21*(3), e2022SW003383. doi: https://doi.org/10.1029/2022SW003383